To be submitted to the 7th International Symposium on Ecohydraulics

Impact of Sediment Overfeeding in Gravel-Bedded River's Salmonid Habitats

Lara M. Ferreira
Instituto Superior Técnico, Lisboa, Portugal, *laraferr@gmail.com*

Abstract: Forest fires can induce severe changes in the morphodynamics and hidrodynamics of mountain rivers, due to the increased sediment production resulting from the erosion of unprotected soil in the catchment, that may occur after these events. Sediment overfeeding can lead to salmonids' habitat degradation, endangering the species. This work aims at the study of the changes in flow hydrodynamics as a result of sand overfeeding in rivers suitable for salmonid spawning, In particular, the study is concerned with the impacts over variables that are better related to oxygen supply to redds: near-bed turbulent and form-induced stresses, velocity profiles and momentum diffusivity. To accomplish this objective, conditions similar to those found in nature, in what concerns the flow and the characteristics of the bed material, were reproduced in laboratory. Instantaneous velocity fields were obtained with Particle Image Velocimetry (PIV). The collected data was analysed and theoretically framed with double-averaged methods. It is shown that in the near-bed region, where the transport of sediments could affect the oxygen supply to redds, the Reynolds stresses are unaffected by bed porosity or sediment transport. However, the form-induced stresses are strongly affected and velocity profiles are conspicuously non-self similar. Eddy viscosity is seemed to decrease in the presence of sediment transport, which may represent an adverse impact for salmonids embryos. Other previously unreported results concerning flow variables in the lower flow layers are presented and discussed.

Key words: Salmonids, sediment transport, habitat degradation, PIV, double-average methods.

1. Introduction

The introduction of fine sediments in spawning sites has been shown to impact negatively on salmonid reproductive success. Salmonid species build their redds in openwork gravel-bedded streams where the interstitial flow is able to supply dissolved oxygen (DO) to the egg pockets and to carry away the metabolic waste disposal. The existence of a fine sediment matrix in redd's gravel framework compromise a successful incubation and can even arm the emergence of alevins (Chapman 1988, Heywood & Walling 2007).

There is no universally accepted relationship between embryo survival and redd grain-size composition, since it is difficult to single out the effect of grain-size composition from the combined effects of the many remaining environmental and ecological variables that describe the flow, water quality and metabolism (Heywood & Walling 2007). However, there is enough evidence that incubation success is inversely related to the percentage in the gravel matrix of grain-sizes smaller than 1.0 mm (Kondolf 2000).

One of the variables that can be negatively impacted by the presence of moving sediment in the lowermost flow layers is the concentration of DO. Vertical profiles of measured DO concentrations show that the near-bed concentration is lower than that of the flow near the free surface. The equilibrium profile of DO in a uniform flow can be calculated from the advection-diffusion mass balance equation if the flow variables, namely vertical mean velocity and eddy diffusivity, and the sources and sinks are known. Especially relevant is eddy viscosity, of which greatly depends the vertical diffusive flux of DO.

The near-bed concentration of DO depends on the vertical diffusive flux; hence is it relevant to know to what extent bedload transport can impact on eddy diffusivity and other flow variables and disrupt the flux of DO to the bed.

The present work was prompted by the concerns that the wildfires that scourged Peneda Gerês national park, Portugal, in 2004, 2005 and 2006 could result in disturbing or eliminating land cover, which, in turn, could cause excess sedimentation in gravel-bedded rivers.

2. Characterization of the physical system

Double-averaged Navier-Stokes equations (DANS) replace Reynolds-averaged Navier-Stokes (RANS) equations for flows over irregular rough boundaries. For steady flows, the DANS (details in Campbell 2005) are

$$\langle \overline{u}_i \rangle \frac{\partial \langle \overline{u}_j \rangle}{\partial x_i} = g_j - \frac{1}{\varphi \rho^{(w)}} \frac{\partial \varphi \langle \overline{p} \rangle}{\partial x_j} - \frac{1}{\varphi} \frac{\partial \varphi \langle \overline{u'_j u'_i} \rangle}{\partial x_i} - \frac{1}{\varphi} \frac{\partial \varphi \langle \widetilde{u}_j \widetilde{u}_i \rangle}{\partial x_i} + \frac{1}{\varphi} \frac{\partial}{\partial x_i} \varphi \left\langle \nu^{(w)} \frac{\partial \langle \overline{u}_j \rangle}{\partial x_i} \right\rangle + \frac{1}{\rho^{(w)} V_f} \int_{S_{\text{int}}} \overline{p}\, n_j \, \mathrm{d}S - \frac{1}{V_f} \int_{S_{\text{int}}} \nu^{(w)} \frac{\partial \overline{u}_j}{\partial x_i} n_i \, \mathrm{d}S + \langle \overline{f}_j \rangle \quad (1)$$

where g_j is the acceleration of gravity, φ is the void function, $\nu^{(w)}$ and $\rho^{(w)}$ are the viscosity and the density of the fluid, respectively, p stands for pressure, u_i for fluid velocity and $\langle \overline{f}_j \rangle$ stands for the force (per unit fluid mass) arising from the interaction between fluid and particles moving as bedload. Equation (1) have been presented by several authors (e.g. Nikora 2001 et al., Campbell 2005) except for the term $\langle \overline{f}_j \rangle$.

Terms $-\rho^{(w)} \varphi \langle \overline{u'_j u'_i} \rangle$ and $-\rho^{(w)} \varphi \langle \widetilde{u}_j \widetilde{u}_i \rangle$ represent the mean Reynolds and the form-induced stress tensor and term $\rho^{(w)} \varphi \langle \nu \partial \langle \overline{u}_j \rangle / \partial x_i \rangle$ is the viscous stress tensor. Terms $1/V_f \int_{S_{\text{int}}} \overline{p}\, n_j \, \mathrm{d}S$ and $-\frac{\rho^{(w)}}{V_f} \int_{S_{\text{int}}} \nu \frac{\partial \langle \overline{u}_j \rangle}{\partial x_i} n_i \, \mathrm{d}S$ are momentum sinks; they stand for pressure and viscous drag per unit mass, respectively. Term $\langle \overline{f}_j \rangle$ was proposed by Ferreira et al. (2008) to account for momentum sink due to sediment transport under the hypothesis of small concentrations of sediment transported as bedload.

In a steady flow under quasi-equilibrium sediment transport inertial effects are negligible to characterize statistically particle movement. Under this hypothesis, the fundamental term to characterize the force that express fluid-particle interactions should be drag on the moving sediment.

The nature of the dominant stresses and momentum sinks can be used as a criterion to characterize the flow structure in coarse-bedded streams. If it can be assumed that the relative submergence is sufficiently high to allow for the existence and overlap of inner and outer regions, the structure of the flow is essentially that of hydraulically rough beds (Townsend 1976, pp. 139-150). Under this assumption Ferreira et al. (2008) proposed a subdivision of the water column into: A – pythmenic layer; B – interfacial layer; C – logarithmic layer; and D – free-surface layer (see Figure 1).

In the pythmenic layer (A), the flow region between crests and troughs of the bed surface and with thickness δ, form-induced and Reynolds stresses coexist if the bedload is small or inexistent. Viscous stresses are negligible since the bed is hydraulically rough. Pressure and viscous drag on the protruding particles act as momentum sinks. Ferreira et al. (2008) postulated that drag forces over moving particles should constitute a fluid momentum sink, feeding on form-induced and Reynolds stresses.

Situated above the particles crests, the interfacial layer (B) is dominated by Reynolds stresses but form-induced stresses and drag on moving particles may be felt in this layer. Pressure and viscous drag on immobile bed elements are not present. Layers A and B will herein be designated as the roughness layer or roughness-influenced layer. Its thickness is k_{sT}.

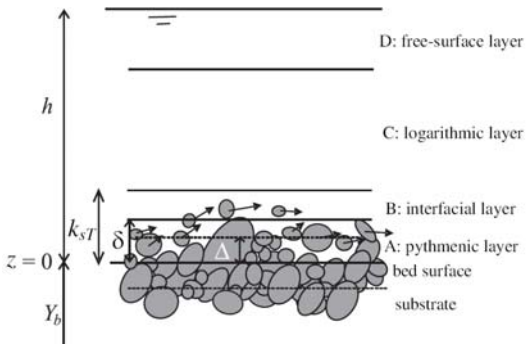

Figure 1. Idealised structure of the flow over hydraulically rough porous poorly sorted gravel-sand beds.

Unlike smooth beds, where drag is of viscous nature, rough beds experience form drag within the roughness elements. Models for the turbulent viscosity are yet to be modified to account for the production-dissipation imbalance due to roughness effects. Mass diffusivity is, for the sake of simplicity, identified with eddy viscosity, or momentum diffusivity (Sanford 1997) which, within the double-averaged theoretical framework, is

$$\nu^{(t)} = -\frac{\varphi \langle \overline{u'w'} \rangle}{\mathrm{d}\langle \overline{u} \rangle / \mathrm{d}z} \quad (2)$$

By potentially affecting Reynolds stresses and shear rates, sediment transport may affect momentum (or mass) diffusivity and, thus, have an impact on the vertical diffusive fluxes of DO, $\partial/\partial z \left(\nu^{(w)} \partial DO/\partial z \right)$, and other ecological variables.

Assuming an overlap of inner and outer regions and making use of similarity arguments regarding

inner and outer geometrical scales, the vertical profile of the longitudinal velocity can be expressed by a logarithmic law (Dittrich and Koll 1997, Ferreira 2005, Franca et al. 2008). In this layer, identified as C in Figure 1, the velocity profile can be expressed by

$$\frac{\langle \overline{u} \rangle}{u_*} = \frac{1}{\kappa} \ln\left(\frac{z-\Delta}{k_{sT}-\Delta} \right) + \frac{\langle \overline{u} \rangle_I}{u_*} \qquad (3)$$

where $u_* = \sqrt{\tau_0 / \rho^{(w)}}$ is the friction velocity, k_{sT} is the thickness of the roughness layer (Figure 1), Δ is the displacement height , $\langle \overline{u} \rangle_I$ is the velocity at the top of the interfacial layer, $\kappa = 0.405$ is the von Kármán constant. Layer D corresponds to the outer region where dissipation exceeds production of TKE.

3. Experimental facilities and instrumentation

The experimental tests were performed in the Recirculating Tilting Flume (CRIV), of the Laboratory of Hydraulics and Environment of Instituto Superior Técnico. The CRIV has a recirculation circuit composed by four tanks, a PVC pipe system and a centrifugal pump. To feed the system with sediments, a conveyor belt was placed on the channel rails at a upstream section. The sediment discharge was controlled by the velocity of the belt and the thickness and width of the sediment streak.

The measurement of the free-surface elevation and the bed topography was done recurring to a 1 mm precision ruler and a 0.1 mm precision point gage, respectively.

The instantaneous flow velocities were measured non-intrusively with Particle Image Velocimetry (PIV). The PIV system used in this experimental work is composed of: (i) laser head and lens, (ii) CCD camera (charge-couple device), (iii) laser beam generator (Solo PIV operator) and (iv) acquisition system and control.

4. Description of the experimental tests

Three laboratorial tests, named S1, S2 and S3, were performed. In order to work within the double-average methodology (DAM), flow profiles were uniformly distributed over an area orders of magnitude a few times larger than the diameter of the bed pebbles (Franca and Czernuszenko 2006). The flume bed is framework-supported (Hogan et al. 1999) in all three tests, i.e. the coarse-gravel elements were in contact forming a stable 3D structure whose voids were empty in test S1 (openwork gravel bed) and filled with sand, in different proportions, in tests S2 and S3.

Test S1 simulated a reference situation inasmuch the flow in the pythmenic and interfacial layers is influenced only by the roughness provided by the gravel bed. In test S2 the porosity was reduced in the substratum but remained fairly identical in the pythmenic layer. Hydrodynamic conditions were influenced by reduced bed porosity and reduced thickness of the pythmenic layer. For test S3, sand content in the bed was increased until its discharge approached capacity transport rates. Test S3 allowed for the characterization of the impact of moving sediment over the turbulent flow in the pythmenic and interfacial layers.

The coarse-gravel sizes in the bed consisted on naturally rounded pebbles, brought from an actual mountain river whose diameters ranged from 0.5 cm to 7 cm, all immobile under the imposed flow conditions. The mean diameter of the sand sizes is $d_{50}^{(s)} = 0.9$ mm and the geometric standard deviation, $\sigma_{D}^{(s)}$ is 2.6. The grain size distribution was plotted.

The grain-size distribution was plotted for both sand and coarse-gravel (details in Ferreira 2008). There is no overlapping between the curves, something not expected to occur in Nature (cf. Kondolf 2000). However, the clear distinction between potentially mobile (sand) and immobile (coarse-gravel) size fractions is expected to render sharper effects, easier to quantify, of sand movement upon flow field descriptors. The bounds of grain-size distribution employed are similar to that found in salmonid spawning areas (Kondolf 2000). The sand fraction is close to the 1.00 mm limit, proposed by Kondolf (2000), whose presence in the bed is harmful for redds.

The bed slope, i_0, the flow discharge, Q, and the gravel framework were kept constant in tests S1 to S3. The adopted values are shown in Table 1. The properties of the gravel framework shown in Table 1 are the mean diameter, $d_{50}^{(g)}$, and the geometric standard deviation, $\sigma_D^{(g)}$.

Table 1. Main hydraulic conditions and framework gravel characteristics.

Q (ls^{-1})	i_0 (–)	$d_{50}^{(g)}$ (mm)	$\sigma_D^{(g)}$ (mm)
23.3	0.00445	28	14

Salmonid species excavate the redds in the transition between pools and riffles in mountain rivers (Chapman 1989, Kondolf 2000). The chosen slope is of the order of magnitude of the slope found in these reaches and used in several laboratory studies. The discharge was chosen to achieve reasonable riffle-pool transition characteristics, namely low to moderate relative submergence, i.e.

$h / d_{50}^{(g)} < 3 - 5$ (Graf & Altinakar 1998) where h is the flow depth.

Prior to test S1, the bed topography was measured with the point gage to render a staggered matrix of elevation samples with a density of 1 sample/cm^2. The result of the bed topography measurement is shown in Figure 2. For each of the tests S2 and S3, additional bed profiles were taken in order to assess the elevation of the sand deposits. It is apparent that the average bed elevation increases from test S1 to S3 due to the sand deposits.

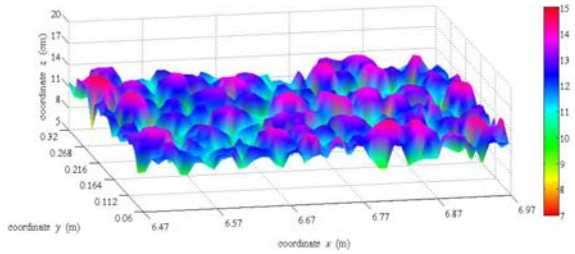

Figure 2. Bed topography of the working area.

Parameters that characterize the bed, are shown in Table 2: elevation of the lowest troughs, $\langle \overline{Y_b} \rangle$; elevation of the highest crests, z_c; bed thickness, δ; mean void fraction in the bed surface, φ_m; bed porosity, λ.

Table 2. Characterization of the bed.

Test	$\langle \overline{Y_b} \rangle$ (m)	z_c (m)	δ (m)	φ_m (–)	λ (–)
S1	0.092	0.146	0.054	0.646	0.38
S2	0.095	0.146	0.051	0.657	0.31
S3	0.107	0.146	0.039	0.720	0.22

Table 3–Mean flow parameters.

Test	Y (m)	h (m)	h_* (m)	U (ms^{-1})
S1	0.246	0.154	0.135	0.570
S2	0.244	0.149	0.131	0.582
S3	0.234	0.127	0.116	0.648

Table 4– Mean flow parameters.

Test	τ_0 $^{(1)}$ (Pa)	u_* $^{(1)}$ (ms^{-1})	τ_0 $^{(2)}$ (Pa)	u_* $^{(2)}$ (ms^{-1})
S1	3.538	0.059	3.614	0.060
S2	4.182	0.065	4.111	0.064
S3	3.218	0.057	3.060	0.057

(1) Calculated from the equation of conservation of momentum in the x direction.

(2) Calculated from the total shear stress profile.

In Table 3, h_*, the equivalent water depth for the calculation of the bed shear stress and U, the depth-averaged mean flow velocity in the longitudinal direction. In Table 4, τ_0 and u_* are the bed shear stress and bed friction velocity and both are calculated from the equation of conservation of momentum in the x direction, (1), and from total shear stress profiles (2).

In Table 5 the following non-dimensional variables pertaining to several flows are shown; Froude number of the mean flow, Fr, Shields' parameter for the gravel and the size fractions, $\theta^{(g)}$ and $\theta^{(s)}$, respectively, Reynolds' number of the mean flow, Re and the bed Reynolds number, Re_*.

Table 5 – Non-dimensional parameters of tests S1 to S3.

Test	Fr (–)	$\theta^{(g)}$ (–)	$\theta^{(s)}$ (–)	Re (–)	Re_* (–)
S1	0.50	0.008	0.263	78580	3320
S2	0.51	0.008	0.299	77964	3312
S3	0.61	0.008	0.223	76606	2181

The determination of the volume of voids in the gravel framework was performed in an apparatus that simulated the flume bed in a 1:1 scale (details in Ferreira 2008). The void fraction of the bed in tests S2 and S3 was obtained from that of test S1 considering the distribution of sand in the interstices. The bed porosity is reduced, from test S1 to S3, due to the increasing presence of sand in the voids of the gravel framework.

In order to account with the void function in the momentum equation, equation (1), best fit curves were adjusted to the void distribution on the three cases. The best fit distribution function is a negative exponential, similar to a Gaussian curve. The mean void fraction in the bed may be determined by:

$$\varphi_m = \int_0^{\delta} \varphi(\eta)\, \mathrm{d}\eta \qquad (4)$$

Tests S1 and S3 were performed under uniform flow conditions. Uniform flow conditions were not achieved during test S2. In this case, the values of the free surface elevation were fitted to a third order polynomial so that it was possible to calculate the free-surface slope from the derivative of that polynomial. It was obtained $\mathrm{d}h/\mathrm{d}x = 0.00013$ at the measuring area ($x = 6.8$). The water elevation was $Y = 24.167$ m.

The value of Re calculated was superior to approximately 700 ($u 4R_* / \nu < 2000$); hence, the open-channel flow is turbulent in all three tests. The bed Reynolds number was superior to 70, thus the bed is hydraulically rough in all three tests. The values of Fr in tests S1 to S2 show that the flow is

subcritical and in the range expected for a pool-riffle transition, as intended.

For hydraulically rough beds, the critical Shields parameter of the sand-sizes becomes $\theta_{cr}^{(s)} = \zeta^{(s)} 0.05$, due to hiding effects (review in Ferreira et al. 2007). It was obtained $\theta_{cr}^{(s)} = 0.093$ and $\theta_{cr}^{(s)} = 0.072$ for tests S2 and S3, respectively. Since the bed is framework-supported, it is assumed that its critical Shields parameters remains 0.005. The sand size is mobile in test S3 ($\theta^{(s)} > \theta_{cr}^{(s)}$) while it remains hidden in test S2 ($\theta^{(s)} < \theta_{cr}^{(s)}$).

It was intended that test S3 would be performed under equilibrium sediment transport conditions. It was also necessary that no bed-forms would develop so that the bed would be comparable to the preceding tests.

After an iterative process, bed equilibrium conditions, eventually emerged. The final equilibrium discharge was $q_b = 4.77 \times 10^{-3}$ ls^{-1}.

In test S2, the voids of the coarse-gravel framework were filled with sand. Since it was required that no movement occurred, the bed was water-worked for several hours to ensure that all mobile sand particles would be transported out of the flume. The remaining sand was effectively hidden by the pebbles in the bed surface.

5. Data collection and analysis

Three longitudinal camera positions were performed in the measuring area, with a minimum of 30 % overlap. This overlap assures that the entire measuring area is covered with redundant information, which is useful to correct measurement errors. In each of the three longitudinal positions, five lateral planes were tested. This ensemble of camera positions and lateral planes defines a measuring area of 21×6 cm^2 (longitudinal×lateral). The lateral dimension is of the order of magnitude of the bed elevation fluctuation and the longitudinal dimension is one order of magnitude greater than the latter. This work is mainly concerned with the near-bed flow, however due to restrictions of the PIV technique one could not measure the entire flow depth with good precision. Hence, the region selected for visualization encompassed the bed surface and the water column with an elevation of approximately 70 % of the flow depth.

The coordinates of each camera image, defined as the pair (i) camera position and (ii) lateral position in the referential of the channel (details in Ferreira 2008).

PIV measurements require the introduction of targets (usually named seeding) in the flow. Pepper grains with 25 to 100 μm were used in this work. This range is in agreement with the typical values of other seeding used in liquids (Raffel et al. 1998). Employing Melling's (1997) theoretical framework it was possible to determine that particles of 80 μm can follow flow turbulent structures up to 15.5 Hz with a 95% level of accuracy. Since the PIV acquisition frequency is 15 Hz, corresponding to Nyquist frequency of 7.5 Hz, it is concluded that these particles are suitable for the present study.

The time-between-pulses, dt, is a relevant variable to control the quality of the PIV measurements, along with the size of the interrogation area and the quantity of seeding; two different values of dt were applied: 700 μs, in test S1 and 750 μs in tests S2 and S3. The trigger rate, f, is the reverse of the time between two consecutive double frames. A trigger rate of 15 Hz, the maximum frequency allowed by the PIV system, was used in all tests: the higher the values of the trigger rate the smaller the flow scales captured. In what concerns the data analysis, the correlations type adopted was adaptive, the validation method was referring to the local median, and an overlap of 50% was done within the interrogation area. For an approach to PIV theory refer to Ferreira 2008.

The instantaneous velocity maps are originally calculated in pixel/s. Furthermore, to obtain data deeper in the bed, the CCD camera was tilted at a 10º angle. To convert velocities from pixel/s to m/s, an algorithm was developed using Direct Linear Transformation (DTL) (details in Ferreira 2008).

The distribution of the sampling points in the measuring area, where profiles are obtained, should be as uniform as possible. The minimum number of profiles, necessary to achieve good quality spatial averages of flow variables over rough beds, has not yet been addressed in research works. Koll (2008, personal communication) used 20 profiles in a study under similar conditions. Initially, 60 sampling points uniformly distributed were sought within the measuring area. The region of influence of each would, on average, be 2.2×10^{-4} m^2, smaller than the plan-view projected area of the median bed surface elements (6.1×10^{-4} m^2). Data was collected in 48, 54 and 56 sampling points for S1, S2 and S3, respectively.

Since the quality of the time-averaged quantities depends on the size of the sample, it was sought that each time-averaged profile would be computed from approximately 1000 maps. On each instantaneous flow map 4 to 6 velocity profiles were sampled. Underlying this procedure is the principal that each profile must be computed from time-independent flow data (details in Ferreira 2008).

The measuring area is confined by a number of fictitious points called frame profiles, distributed as if they were actual flow profiles. The regions of influence of each profile (including the fictitious points and those of the frame) are the areas of the Voronoï polygons of the mesh of profiles (Figure 3).

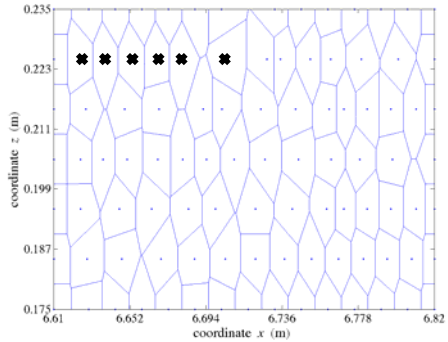

Figure 3 – Areas of influence of the 54 sampled profiles of test S2 computed from its Voronoï polygons. Crosses represent the sampling point for which data was faulty.

The number of points in the vertical profiles depends on the size of the interrogation area and on the overlapping resulting in an order of magnitude of 100 points per profile. The vertical spacing of the points depends on the calibration factor and, hence, the images taken closer to the wall have a better resolution. On average, the vertical spacing of the points in the profiles is 0.5 mm. This also means that the velocity vector at each vertical position is the result of a space-averaging process within an interrogation area of 0.5×0.5 mm, on average.

6. Results and discussion

6.1 Near-bed pressure distribution

In a gradually-varied flow, longitudinal gradients are small compared with vertical gradients. The flow is turbulent and, hence, viscous stresses are negligible.

The vertical velocity distribution is small throughout the water column. The vertical convective acceleration, estimated from distribution of the mean vertical velocity (Figure 4), is about $0.3\,\mathrm{ms}^{-2}$, considerably smaller than the acceleration of gravity. Thus, this term will be neglected. The near bed pressure distribution obeys (details in Ferreira 2008)

$$\varphi(z)\left\langle \overline{p}\right\rangle(z) = \rho^{(w)} g \left\{\varphi\right\}_z^{\delta} (\delta - z) + \rho^{(w)} g (h - \delta) - \rho^{(w)} \varphi(z)\left(\left\langle \overline{w'^2} \right\rangle(z) + \left\langle \tilde{w}^2 \right\rangle(z) \right) + F(\varphi) \quad (5)$$

Equation (5) shows that the influence of sediment transport on the pressure distribution can occur through the form-induced normal stresses, the Reynolds stresses and void fraction. The void fraction function is not significantly altered by the existence of near bed transport. Hence, at a given height above the bottom, the deviation from the hydrostatic profile, due to sediment transport, is limited to the impacts in the normal stresses. Figures 4 and 5 show the normal vertical mean Reynolds and form-induced stresses.

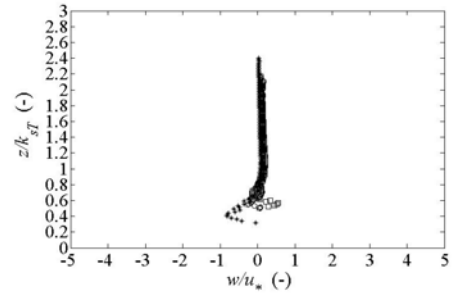

Figure 4 – Non-dimensional double-averaged mean vertical velocity ($\left\langle w \right\rangle / u_*$). Open circles (○), open squares (□) and asterisks (✱) stand for tests S1, S2 and S3, respectively.

Figure 5 shows that the mean normal vertical Reynolds stresses seem unaffected by sediment transport. The magnitude of form-induced vertical normal stresses decreases as the sand content in the bed increases (Figure 6). This should be caused by restrictions to the fluctuations of the vertical velocity as the coarse elements in the bed become immersed in sand.

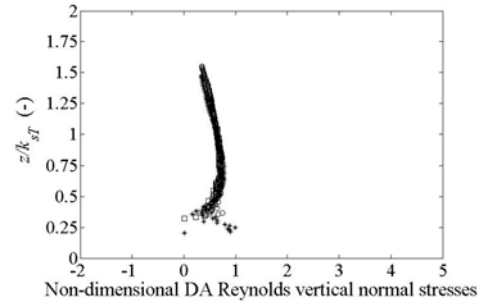

Figure 5 – Non-dimensional double-averaged Reynolds vertical normal stresses $\left\langle \overline{w^2} \right\rangle / u_*^2$. Symbols as in Figure4.

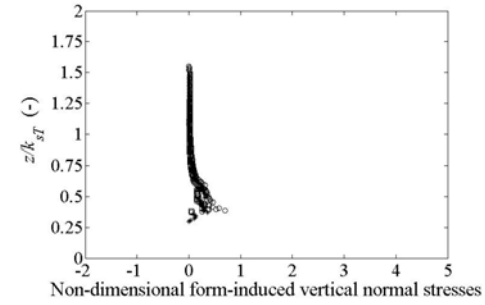

Figure 6 – Non-dimensional form-induced vertical normal stresses ($\left\langle \tilde{w}^2 \right\rangle / u_*^2$). Symbols as in Figure 4.

It is concluded that the pressure distribution may be indirectly affected by sediment transport in the pythmenic layer as a result of changes in the normal vertical form-induced stresses. This impact is of second order, relatively to the dominant hydrostatic term.

6.2 Shear stress distribution and bed shear stress

The integration of equation (1) in the longitudinal direction revelal that the total force exerted on the bed and moving particles (bed shear stress) by the fluid flow is

$$\tau_0 = -\rho^{(w)} g h_* \left(\frac{\mathrm{d}\left\langle \overline{Y_b} \right\rangle}{\mathrm{d}x} + \frac{h}{h_*} \frac{\mathrm{d}h}{\mathrm{d}x} \right) + \rho^{(w)} \lambda \left(\left\langle \overline{u'w'} \right\rangle (0) + \left\langle \tilde{u}\tilde{w} \right\rangle (0) \right) = D_P + D_v + F_x \quad (6)$$

where D_P, D_V and F_x stand for pressure drag, viscous drag and fliud-particle interaction, respectively. It is clear from equation (6) that the effects of sediment transport occur through term F_x. At constant bed shear stress, an increase in F_x must represent a decrease of form drag. The profiles of the total and Reynolds shear stresses obtained for tests S1 to S3 are shown in Figure 7.

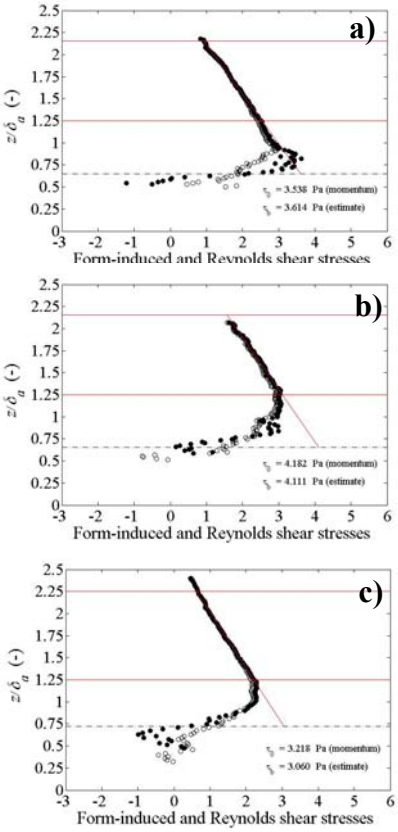

Figure 7 – Form-induced and Reynolds shear stresses and linear regression for the computation of the bed shear stress, τ_0 and τ_b. a) Test S1; b) Test S2; c) Test S3. White and black makers stand for mean Reynolds and total stresses, respectively.

The computation of the bed shear stress can be carried out by intersecting the linear profile with an adequate reference level. This reference level, $h_* = h - \delta\left(1 - \varphi_m\right)$, can be found by integrating the equation of momentum in the longitudinal direction between zero and the flow depth.

The value of the bed shear stress decreases from test S1 to test S3, due to the smoothening effect provided by the existence of moving sand in the pythmenic layer. Exception made for test S2, where the bed shear stress rises due to non uniform flow conditions.

6.3 Form-induced and mean Reynolds stresses

It is observed in Figure 7 that, for a given slope and water discharge, the bed shear stress is smaller when there is near-bed sand transport. This effect is mainly due to bed smoothening: the roughness elements become immersed in a layer of moving sand and, as a result, the thickness of the bed decreases. Therefore, viscous and pressure drag decrease because the total area of fluid-solid interface decreases. Drag on moving sand particles is, due to the small concentration of moving particles, not enough to raise the values of the bed shear stress.

The interaction force between moving sediment and fluid is an extra sink in the momentum equation. An increase of this term, at constant bed shear stress must represent a decrease in either or all mean Reynolds stresses, form-induced stresses or form drag (equation 6). This is an especially relevant issue for the characterization of environmental fluids since vertical turbulent transport of momentum (Reynolds stresses) should be related to fluxes of ecologically relevant variables. Figures 8 and 9 show mean Reynolds stresses and form-induced stresses and allow for the characterization of the effects of sediment transport.

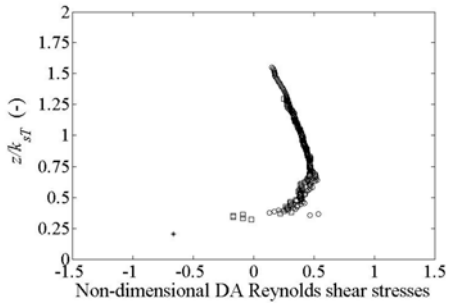

Figure 8 – Non-dimensional double-averaged Reynolds shear stresses ($\langle u'w' \rangle / u_*^2$). Symbols as in Figure 4.

Mean Reynolds shear stresses seem unaffected by sediment transport (Figure 8). Considering the drag force on near-bed moving particles a sink in the equation of momentum in the longitudinal direction

and that mean Reynolds stresses are unaffected by sediment transport, it is concluded that drag on moving particles feeds on form-induced stresses and, presumably, on form drag.

As seen in Figure 9, form-induced shear stresses are smaller when the bed undergoes sediment transport. The profile of form-induced shear stresses is typical the one of rough beds in test S1 (openwork gravel bed), showing an alternation between a positive and a negative maxima in the pythmenic layer.

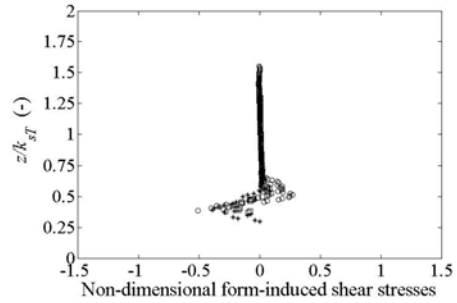

Figure 9 – Non-dimensional form-induced shear stresses ($\langle \tilde{u}\tilde{w} \rangle / u_*^2$). Symbols as in Figure 4.

In test S2 (increased sand content in the bed) the positive maximum is attenuated. In test S3 (sand transport in the pythmenic layer), the positive maximum disappears; form-induced shear stresses become negative throughout the pythmenic layer. This confirms that drag on moving elements is feeding on form-induced stresses rather than on mean Reynolds stresses. The direct effect on form drag is not assessable.

Figures 10 and 11 show longitudinal normal mean Reynolds and form-induced stresses, respectively.

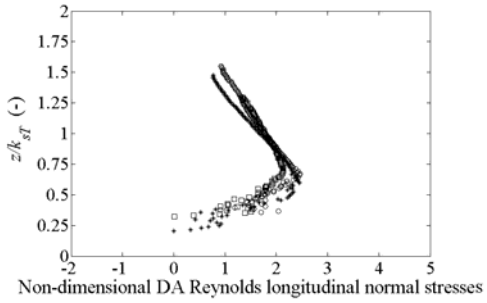

Figure 10 – Non-dimensional double-averaged Reynolds longitudinal normal stresses ($\langle u'^2 \rangle / u_*^2$).Symbols as in Figure 4.

It is verified in Figure 10 that mean normal Reynolds stresses, as before the shear stresses, are not significantly affected by sediment transport. Unlike vertical normal form-induced stresses, whose magnitude decreases with sediment transport, longitudinal form-induced stresses (Figure 11) appear to be essentially unaltered as the sand content in the bed increases and sand transport develops.

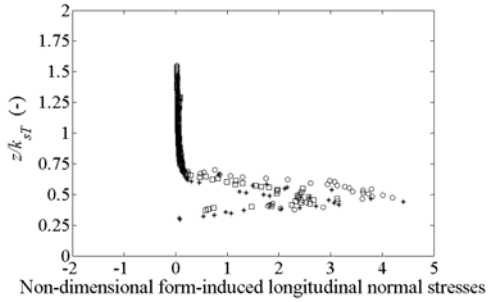

Figure 11 – Non-dimensional form-induced longitudinal normal stresses ($\langle \tilde{u}^2 \rangle / u_*^2$).Symbols as in Figure 4.

6.4 Double-averaged longitudinal velocity profile

In open-channel flow over hydraulically rough beds with large enough relative submergence, the longitudinal velocity profile may be fitted to logarithmic law above the roughness-influenced layer (Dittrich and Koll 1997, Nikora et al. 2001). For rough mobile beds, Ferreira et al. (2008) noted that the parameters of the log-law change with the increase of bed mobility and that, as a consequence, the velocity profiles could not be self-similar.

Figure 12 shows the velocity profiles obtained for tests S1 to S3. It is clear that a log-law can indeed be fitted to the measured mean longitudinal velocity profiles.

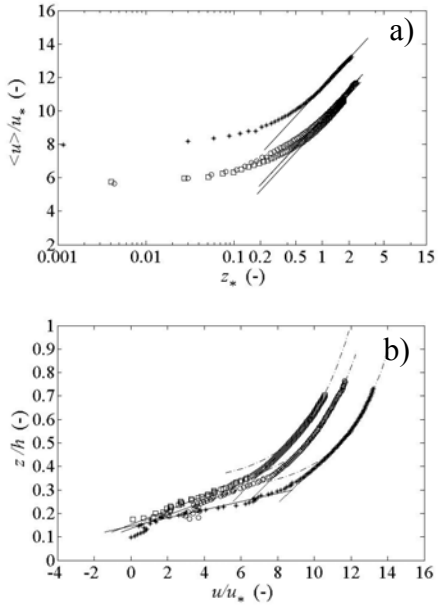

Figure 12 – Double-averaged mean longitudinal velocity profiles. a) Logarithmic plot showing theoretical log-law; b) Full profile showing logarithmic and bi-lineal reaches. Symbols as in Figure 4.

It was verified that there is no universal self-similar log law when the velocity profile is

normalized by the bed friction velocity; the profile for test S3, influenced by sediment transport, does not collapse over the same curve of profiles for S1 and S2. It is also clear from Figure 12 that the velocity profile in the roughness layer can be expressed by a bi-linear law, i.e. two linear reaches with different slopes. The linear profile in the interfacial layer was already reported by Nikora et al. (2001), Ferreira (2005) and Ferreira et al. (2006). The linear reach in the pythmenic layer is a previously unreported feature.

6.5 Eddy viscosity

The eddy viscosity can be calculated as the ratio of the Reynolds stresses and the shear rate.

Figure 13 shows eddy viscosity profiles of the eddy viscosity for tests S1 to S3 calculated with equation (2). The turbulent viscosity decreased in test S3, relatively to the values of S1 and S2, which is mainly an effect of the non-self-similarity of the velocity profile. Vertical fluxes of mass may be affected, in the hypothesis that mass diffusivity is approximately equal to momentum diffusivity.

The equation of conservation of the mass of ecologically relevant variables, such as DO, obeys an advection-diffusion equation

$$\frac{\partial DO}{\partial t} + u_i \frac{\partial DO}{\partial x_i} = \frac{\partial}{\partial x_i} \varepsilon \frac{\partial DO}{\partial x_i} - \gamma \qquad (7)$$

where $\varepsilon \approx \nu^{(t)}$ stands for mass diffusivity and γ for the rate of production/reaction/dissipation of DO.

One observes herein that advective fluxes of DO should be of little importance since the vertical velocity profile is small throughout the water column irrespectively of the presence of sediment transport.

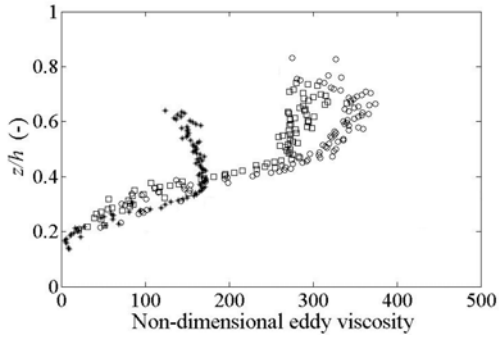

Figure 13 – Non-dimensional eddy viscosity $(\nu^{(t)}/(k_s u_*))$. Symbols as in Figure 4.

However, the vertical diffusive flux of DO, $\partial/\partial z\left(\nu^{(w)}\, \partial DO/\partial z\right)$, may be affected by the presence of near-bed sand transport since the eddy viscosity apparently decreases with sediment transport. Hence, the main adverse impact for salmonid egg incubation may be a reduction of the concentration of DO in the near bed region due to a reduction of its vertical diffusive flux.

7. Conclusions

For a given slope and water discharge, the bed shear stress is smaller when there is near-bed sand transport. This effect is mainly due to bed smoothening. Therefore, viscous and pressure drag decrease because the total area of fluid-solid interface decreases. Drag on moving sand particles is, due to the small concentration of moving particles, not enough to raise the values of the bed shear stress.

Reducing porosity alone does not appreciable affect the value of the bed shear stress. This should be related to the fact that the bed thickness remains essentially unaltered and hence form drag is not affected.

The pressure distribution may be indirectly affected by sediment transport in the pythmenic layer as a result of changes in the normal vertical form-induced stresses. This impact is of second order, relatively to the dominant hydrostatic term. At the bottom of the pythmenic layer, there is no effect of sediment transport as the normal stresses tend to zero.

Mean Reynolds stresses, both shear and normal, seem unaffected by sediment transport. This result is especially relevant to understand flow dynamics in the longitudinal direction. The result that mean Reynolds stresses are unaffected by sediment transport reveals that drag on moving particles feeds on form-induced stresses.

Form-induced shear stresses are smaller when the bed undergoes sediment transport. The profile of form-induced shear stresses is typical of rough beds in test S1 (openwork gravel bed), showing an alternation between positive and negative maxima in the pythmenic layer. In test S2 (increased sand content in the bed) the positive maximum is attenuated. In test S3 (sand transport in the pythmenic layer), the positive maximum disappears; form-induced shear stresses become negative throughout the pythmenic layer. This confirms that drag on moving elements is feeding on form-induced stresses rather than feeding on mean Reynolds stresses.

The magnitude of form-induced vertical normal stresses decreases as the sand content in the bed increases. This should be caused by restrictions to the fluctuations of the vertical velocity as the coarse elements in the bed become immersed in sand. Longitudinal form-induced stresses appear to be essentially unaltered as the sand content in the bed increases and sand transport develops.

The profile of the mean longitudinal velocity appears to conform to the classical log-law description above the roughness-influenced layer. However, sand transport seems to render the velocity

profiles non-self-similar, which confirms other researchers' results.

The longitudinal velocity profile in the roughness layer seems to be double-linear. A linear reach in the interfacial layer (previously reported) is articulated with a different linear reach in the pythmenic layer.

The vertical velocity profile is essentially zero in the water column independently of the sand content in the bed and of the existence of moving particles. The small differences in the values of this variable, in the pythmenic layer, encountered among the tests, are not amenable to discussion due to its small magnitude.

The turbulent viscosity can be potentially affected by near-bed sediment transport. In fact, it was observed that the turbulent viscosity decreased in test S3, relatively to the values of S1 and S2, which is mainly an effect of the non-self-similarity of the velocity profile. Vertical fluxes of mass may be affected, in the hypothesis that mass diffusivity is approximately equal to momentum diffusivity.

In what concerns ecologically relevant variables, such as DO, their vertical flux may be affected by the presence of near-bed sand transport, since momentum diffusivity (eddy viscosity) apparently decreases with sediment transport. The main adverse impact for salmonid egg incubation may be a reduction of the concentration of DO in the near bed region due to a reduction of its vertical flux.

References

Campbell, L. J. (2005). *Double-Averaged Open-Channel Flow over Regular Rough Beds*. Department of Engineering University of Aberdeen. University of Aberdeen.

Chapman, D. W. (1988). Critical Review of Variables Used to Define Effects of Fines in Redds of Large Salmonids. *Transactions of the American Fisheries Society*: Vol. 117, No. 1 pp. 1–21.

Dittrich, A. and Koll, K. (1997). Velocity field and resistance of flow over rough surface with large and small relative submergence. *Int. J. Sediment Res*.: Vol. 12, No.3, pp. 21-33.

Ferreira, L (2008). *Impact of Sediment Overfeeding in Gravel-Bedded River's Salmonid Habitats*. MSc thesis. Instituto Superior Técnico. Universidade Técnica de Lisboa. Lisbon.

Ferreira, R. M. L.; Franca, M. J.; Leal, J. G. A. B. (2007). Laboratorial and theoretical study of the mobility of gravel and snd mixtures. *Proc. 5th RCEM 2007*, Dohmen-Janssen & Hulscher (eds), pp: 531-539.

Ferreira, Rui. M. L.; Franca, Mário. J.; Leal, João. G. A. B. (2008). Flow resistance in open-channel flows with mobile hydraulically rough beds. *River Flow 2008* Altinakar et al. (eds). Vol. 1, pp. 385-394.

Ferreira, R. M. L. (2005). *River Morphodynamics and Sediment Transport. Conceptual Model ad Solutions*. PhD Thesis. Instituto Superior Técnico. Universidade Técnica de Lisboa.

Franca, M.J., Ferreira, R.M.L. and Lemmin, U. (2008). Parameterization of the logarithmic layer of double-averaged streamwise velocity profiles in gravel-bed river flows. *Advances in Water Resources*. 31:6 (2008) 915-925

Franca M.J. and Czernuszenko W. (2006). Equivalent velocity profile for turbulent flows over gravel riverbeds, in *River Flow 2006*, R.M.L. Ferreira et al (eds) Taylor & Francis Ltd (ISBN 0415408156).

Graf, W. H. & Altinakar, M. S. (1998). *Fluvial Hydraulics: Flow and Transport Processes in Channels of Simple Geometry*, John Wiley & Sons Chichester, UK.

Heywood, M. J. T. & Walling, D. E. (2007). The sedimentation of salmonid spawning gravels in the Hampshire Avon catchment, UK: implications for the dissolved oxygen content of intragravel and embryo survival. *Hydrological Processes*: Vol. 21, pp. 770-788.

Hogan, D. L.; Bird, S. A. & Hassan M. A. (1999). Spatial and temporal evolution of small coastal gravel-bed streams: influence of forest management on channel morphology and fish habitats in gravel-bed rivers in the environment. In: C. Klingeman, R.L. Beschta and P.D. Komar, Editors, Water Resources Publications.

Kondolf, G. M. (2000). Assessing Salmonid Spawning Gravel Quality. *Transactions of the American Fisheries Society*: Vol. 129, No. 8, pp. 262-281.

Melling, A. (1997). Tracer particles and seeding for particle image velocimetry. Measurement Science and Technology: Vol. 8, pp. 1406-1416.

Nikora, V.; Goring, D. McEwan & I. Griffiths, G. (2001). Spatially Averaged Open-Channel Flow over Rough Bed. *J. of Hydraul. Eng.*: Vol. 127, No. 2, pp.123-133.

Raffel, M.; Willert, C. E. & Kompenhans, J. (1998). *Particle Image Velocimetry, a Practical Guide*, Springer-Verlag, Berlin, Germany.

Sanford, L. P. (1997). Turbulent mixing in experimental ecosystem studies. *Marine Ecology Progress Series*: Vol. 161, pp. 265-293.

Townsend, A. A. (1976). *The structure of Turbulent Shear Flows*. 2nd Edition. Cambridge University.